Modelling of CO_2 decompression across the triple point

Wentian Zheng[†], Haroun Mahgerefteh* [†], Sergey Martynov[†], Solomon Brown[‡]

[†] Department of Chemical Engineering, University College London, London WC1E 7JE, U.K.

[‡] *Department of Chemical and Biological Engineering, The University of Sheffield, Mappin*

Street S1 3JD, U.K.

The formation of significant quantities of solid CO_2 as a result of surpassing its triple point during rapid decompression of CO_2 pipelines employed as part of the Carbon Capture and Sequestration (CCS) chain can present serious operational and safety challenges. In this paper, the development, testing and validation of a rigorous Computational Fluid Dynamics (CFD) flow model for predicting solid CO_2 formation during decompression is presented. Multiphase flow is modelled by assuming homogeneous equilibrium, and the pertinent thermodynamic data are computed using real-fluid equations of state. The flow model is validated against pressure and temperature data recorded during the decompression of an extensively instrumented 144 m long, 150 mm i.d. CO_2 pipe initially at 5.25 ^{o}C and 153.3 bar. For the conditions tested, the simulated results indicate CO_2 solid mass fractions as high as 35% at the rupture plane, whose magnitude gradually decreases with distance towards the pipe's intact end.

1. INTRODUCTION

CO_2 is widely recognised as the major contributor to global warming due to its widespread emissions primarily from industrial sources and coal-fired power plants [1]. Carbon Capture and Sequestration (CCS) aimed at the capture of anthropogenic CO_2 and its long-term storage in geological formations has been identified as a key player in effectively mitigating such emissions. Given that capture locations are often not collocated with the storage sites, the transportation of captured CO_2 using high-pressure pipelines offer the best practical solution for on-shore CO_2 transport.

During the course of the CO2PipeHaz European Commission FP7 project [2], a series of experimental investigations involving the release of compressed CO_2 from a fully instrumented 256 m long, 233 mm i.d. pipeline were conducted. This work was initiated in the first instance in view of the significant amounts of CO_2 involved during its pipeline transportation (several hundred tonnes per year). CO_2 at concentrations greater than 7% v/v is toxic [3]. As such, reliable and validated mathematical models for predicting the transient outflow into the environment and mapping the dispersion behaviour of the escaping CO_2 cloud in the event of accidental pipeline failures are essential components of the risk management. Such data form the basis of determining the minimum safety distances to populated areas and emergency response planning.

An interesting and important observation made from the CO2PipeHaz FP7 pipeline rupture tests [2] was that the rapid expansion-induced cooling of the CO_2 often resulted in surpassing its triple point temperature 216 K [4], leading to solid CO_2 (commonly known as 'dry ice') formed inside the pipeline as can be observed in the photographs (figure 1) taken in the CO2PipeHaz Full-Bore Rupture (FBR) test performed using pure CO_2 initially at 53 bar and 2 $^{\circ}$C.
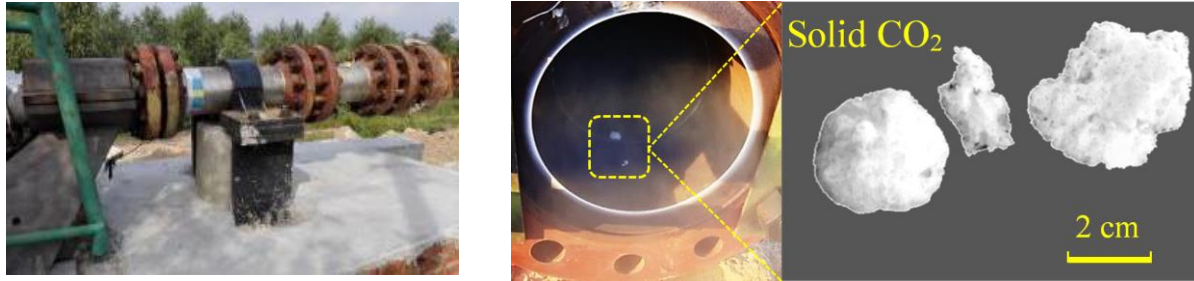
(a)   (b)

Figure 1: Photographs of the release end of the CO2PipeHaz blowdown test pipeline (a) and lumps of solid CO_2 formed within the pipe in the FBR test (b). Photographs courtesy of Dalian University of Technology.

This observation has significant operational and safety implications. In practice, CO_2 pipelines will require depressurisation following emergencies or for routine maintenance purposes. The formation of any significant amounts of solids within the pipeline may result either in its blockage (especially along restrictions such as bends) or, more likely, the blockage of the emergency pressure relief valves, leading to an over-pressurisation and possible pipeline rupture [5,6]. Indeed, Huang et al. [7] reported pressure relief valve blockage during the throttling of CO_2. Similar concerns are also relevant in hydrocarbon transportation pipelines, albeit as a result of solid hydrate formation along the pipe [8]. Hydrate formation is not considered as an issue in the case of CO_2 pipelines given the amount of water permitted must be restricted to no more than 500 ppm [9] to avoid the risk of pipeline corrosion due to the formation of carbonic acid.

Additionally, the accumulation of solid CO_2 near the release point and its subsequent protracted sublimation will have a profound impact on the risk profile of the migrating CO_2 cloud, ultimately dictating the minimum safety distance to populated areas [10]. Finally, any undiscovered solid CO_2 accumulated along the depressurised pipeline may expose personnel to dangerously high concentrations of the subliming CO_2 during maintenance inspection.

As such the ability to reliably predict depressurisation conditions leading to the risk of solid CO_2 formation, and if relevant its quantity, is highly desirable.

To date, although some work has been reported for modelling the depressurisation of CO_2 pipelines, including multiphase flow behaviour (see for example [11–14]), such studies have been mainly limited to depressurisation up to the CO_2 triple point.

In a recent study [15], as part of the CO_2PipeHaz project [2], we developed a vessel blowdown model based on the Homogeneous Equilibrium Mixture (HEM) assumption accounting for CO_2 liquid, vapour and solid phases. Incorporating the extended Peng-Robinson Equation of State (ePR EoS) [16] to deal with solid phase CO_2, we successfully simulated the depressurisation trajectory of 256 m long, 233 mm i.d. CO_2 pipe, including the observed temporal pressure stabilisation when crossing the triple point. However, given that our vessel blowdown model did not account for spatial pressure variation in the containment, its application is restricted to relatively small-puncture releases in sufficiently short pipelines where the variations in the flow properties along the pipeline are insignificant.

Hammer et al. [17] presented a CFD pipeline flow model where the CO_2 vapour-liquid-solid mixture was also assumed to be at thermal and mechanical equilibrium (i.e. HEM). As part of the model verification, a Riemann problem test was performed to predict the wave structure (e.g. the evolution of an initial pressure profile with a step change) in the three-phase flow, and anomalous waves were observed at the CO_2 triple point. Given that fluid flow (e.g. pipe flow) may be viewed as a non-linear superposition of local Riemann problem solutions [18], such waves can be expected to greatly affect the pipe flow during decompression.

Hammer et al. [17] also presented simulation data relating to a hypothetical full-bore pipeline rupture decompression scenario using their CFD model. Much the same as Martynov et al. [15], a

pressure plateau at the triple point was reported. In their later publication [19], a comparison between the model predictions and the measured pressure and temperature data during a CO_2 pipeline decompression test was presented.

In conclusion, despite the significant potential risks associated with solid CO_2 formation following the rupture or controlled blowdown of high-pressure CO_2 transportation pipelines, there are no reliable and validated decompression flow models available for predicting the likelihood or the extent of CO_2 solid formation.

This paper details the development, verification and validation of a CO_2 pipeline decompression model for predicting CO_2 solid formation at any time and distance along the depressurising pipeline. The paper is organised as follows. In Section 2, the flow model equations are summarised, including the conservation laws and closure models for fluid/wall heat transfer and friction. In addition, a general discussion of the elementary wave solution of the governing hyperbolic conservation equations is provided to aid the analysis of the simulated results. Also, the boundary conditions and the pertinent fluid physical properties prediction methods such as the speed of sound for two-phase (liquid-vapour and solid-vapour) and three-phase (vapour-liquid-solid) CO_2 mixtures are presented. The numerical technique for solving the conservation equations and their enclosure is given next in Section 3. In Section 4, the verification of the flow model is carried out by performing a Riemann problem test to predict the wave propagation in a vapour-liquid-solid CO_2 flow. The resulting wave structure is discussed in detail with a particular focus on the impact of solid CO_2 formation. This is followed by model validation against experimental data obtained from a large-scale CO_2 pipeline depressurisation test. Conclusions are drawn in Section 5 along with proposals for future work.

2. THEORY

2.1 Flow model. In order to describe the depressurisation of CO_2 in a pipeline upon failure, the following set of conservation equations is applied based on the HEM assumption [11,20]:

$$\frac{\partial}{\partial t}U + \frac{\partial}{\partial x}F(U) = \boldsymbol{\Psi} \tag{1}$$

where U is the vector of the conservative variables, F is the vector of the corresponding flux functions, and $\boldsymbol{\Psi}$ is vector of source terms, defined as:

$$U = \begin{pmatrix} \rho \\ \rho u \\ \rho(u^2/2+e) \end{pmatrix}, \quad F = \begin{pmatrix} \rho u \\ \rho u^2 + p \\ u(\rho(u^2/2+e)+p) \end{pmatrix}, \quad \boldsymbol{\Psi} = \begin{pmatrix} 0 \\ -2f\rho u^2/D \\ (-2f\rho u^3 + 4\dot{q})/D \end{pmatrix} \tag{2}$$

Here p is the pressure, u is the velocity, f is the Fanning friction factor which in the present study is calculated using Chen's correlation [21]. D, is the pipeline diameter, and $\dot{q}$ is the heat flux from the pipe wall to the in-pipe fluid. ρ and e are respectively the mixture density and specific internal energy in turn defined as:

$$\rho = \left(\sum_k y_k/\rho_k\right)^{-1}, \quad e = \sum_k y_k e_k \tag{3}$$

where y_k is the mass fraction of phase k ($k = v$, l and s).

For rapid depressurisation-induced liquid flashing, nucleate boiling is assumed to be the dominating heat transfer mechanism [22,23]. As such, $\dot{q}$ is estimated following Rohsenow's correlation [24]:

$$\dot{q} = \mu_l h_{fg}\left(\frac{g(\rho_l - \rho_g)}{\sigma}\right)\left(\frac{C_{p,l}(T_w - T)}{0.013 h_{lg} Pr_l}\right)^3 \tag{4}$$

where μ, σ, h_{lg}, $C_{p,l}$ and Pr_l are respectively the viscosity, the surface tension, the latent heat of vaporisation, the heat capacity and the Prandtl number of the liquid phase, which are calculated

using NIST models [25]. T_w is the wall temperature governed by the lumped thermal capacity model [15]:

$$\dot{q} = \rho_w C_w \delta_w \frac{\partial T_w}{\partial t}$$

(5)

where ρ_w, C_w and δ_w are the density, heat capacity and thickness of the pipe wall respectively.

2.2 Hyperbolicity and wave structure of the solution. Assuming the source term in Eq. (1) does not interfere the wave structure [20], the system reduces to the Euler equations of gas dynamics:

$$\frac{\partial}{\partial t} U + \frac{\partial}{\partial x} F(U) = 0$$

(6)

The three eigenvalues of the Jacobian matrix of F are [26]: $\lambda_1 = u - c$, $\lambda_2 = u$, $\lambda_3 = u + c$, where c is the sound speed in the fluid. When the eigenvalues are real the system described by Eq. (6) is hyperbolic and exhibits wave behaviour. In this case, the eigenvalues are the wave speeds of the three characteristic waves which form the classical wave structure of the solution, as schematically shown in figure 2.
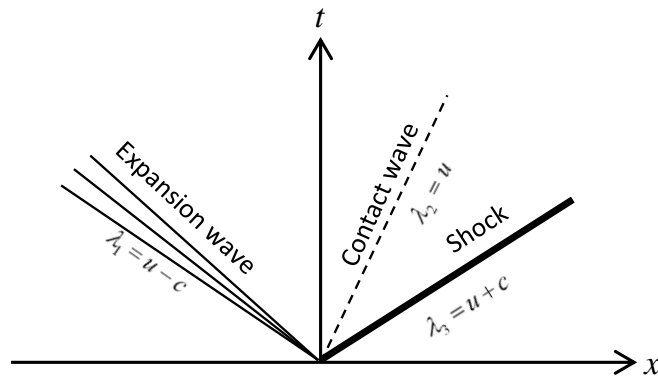

Figure 2: Schematic representation of the classical wave structure from solving the Euler equation of gas dynamics.

As may be observed in figure 2, a left-going expansion wave and a right-going shock are separated by a contact wave. It should be noted that the classical wave structure in figure 2 applies only to the case when isentropes in the pressure-specific volume (*p-v*) thermodynamic plane, $(\partial p/\partial v)_s$ remain convex and smooth [18]. Since isentropes are directly related to speed of sound through:

$$c = \sqrt{\left(\frac{\partial p}{\partial \rho}\right)_s} = \sqrt{\left(\frac{\partial p}{\partial v}\frac{\partial v}{\partial \rho}\right)_s} = v\sqrt{\left(\frac{\partial p}{\partial v}\right)_s} \tag{7}$$

the speed of sound as a result must be continuous.

As shown by Menikoff and Plohr [18], isentropes are smooth and convex if and only if the fundamental derivative, defined below remains positive everywhere in the *p-v* plane:

$$\varsigma = -\frac{1}{2}v\frac{\left(\partial^2 p/\partial v^2\right)_s}{\left(\partial p/\partial v\right)_s} \tag{8}$$

On the other hand, non-classical wave structure, also known as anomalous wave structure, arises when ς becomes zero or undefined (often referred as 'vanish'). This typically happens at phase transition boundaries where isentropes (in *p-v* plane) exhibit a discontinuous change in the slopes (and hence the speed of sound). The resulting anomalous waves can be further categorised into a split rarefaction, if upon crossing the phase boundary the relevant isentrope remains convex ($\varsigma > 0$) and a composite wave comprised of a shock attaching to a rarefaction wave, if the isentrope becomes concave.

For example, Menikoff and Plohr [18] showed that in real fluids, where isentropes convexity is preserved upon crossing the phase transition boundary in *p-v* plane, the liquid evaporation induced by decompression would produce a pair of rarefaction waves splitting at the saturation pressure.

2.3 Boundary conditions. In order to close Eq. (1) to enable their numerical solution, appropriate boundary conditions at the closed end of the pipeline, and the multi-phase outflow at the rupture end need to be specified. In particular, at the closed end, the velocity is set to zero, while for scalar variables (e.g., pressure and density), zero-gradient extrapolation is applied.

Turning to the rupture end, where the flow is expected to be choked (sonic) during the most part of the decompression process, the boundary condition is determined from analysis of local waves of the governing equations [27]. In the case of sonic flow, the local left-running pressure wave (see figure 2) is stationary. By integrating the corresponding Riemann invariant, the following relation can be derived [27]:

$$u_{bc} = u_{mx} - \int_{P_{mx}}^{P_{bc}} \frac{dp}{\rho c} \tag{9}$$

where the subscript, mx represents the last numerical cell at the pipeline release end. By assuming isentropic flow condition (i.e. $s_{bc} = s_{mx}$), ρ and c can be computed at a given pressure and entropy (using the pressure-entropy flash calculations). Knowing the outflow is sonic (i.e. $u_{bc} = c$), Eq. (9) is thus closed (the only remaining unknown is p_{bc}). The corresponding discharge mass flowrate can be calculated as $\dot{m} = \rho_{bc} u_{bc} \left(\pi D^2 / 4 \right)$.

2.4 Physical properties. In order to predict the thermodynamic properties of CO_2 required for the HEM flow model, dedicated correlations are employed based on the GERG 2004 EoS [28] and ePR EoS [16]. The former EoS is applied for the prediction of CO_2 liquid-vapour mixture owning to its much higher accuracy over the cubic EoS [28]. Below the triple point, the ePR EoS is employed which has been shown to produce good accuracy in handling solid phase CO_2 [16].

The HEM speed of sound of a compressible single-phase or multiphase fluid is defined in Eq. (7). In the case of two-phase mixture, substitution of Eq. (3) into Eq. (7) gives the following expression for the speed of sound [20]:

$$c = \frac{1}{\rho} \sqrt{1 \Bigg/ \left[\left(\frac{y_v \gamma_v}{\rho_v} + \frac{y_l \gamma_l}{\rho_l} \right) - 2 \left(\frac{y_v \beta_v}{\rho_v} + \frac{y_l \beta_l}{\rho_l} \right) \left(\frac{1/\rho_v - 1/\rho_l}{s_v - s_l} \right) + \frac{\overline{C_p}}{T} \frac{(1/\rho_v - 1/\rho_l)^2}{(s_v - s_l)^2} \right]} \tag{10}$$

where $\overline{C_p}$ is the average mixture heat capacity; while γ and β are respectively the isentropic compressibility and thermal expansion factor of each phase:

$$\forall k = v, l; \qquad \gamma_k = -\rho_k \left(\frac{\partial 1/\rho_k}{\partial p} \right)_s = -\frac{c_k}{\rho_k^2} \tag{11}$$

$$\forall k = v, l; \qquad \beta_k = -\frac{1}{\rho_k} \left(\frac{\partial \rho}{\partial T} \right)_{k,p} \tag{12}$$

With regards to a HEM vapour-liquid-solid mixture at the triple point, following Eq. (7), the speed of sound is zero (as the pressure stays constant at the triple point). This implies that waves cannot propagate upstream of the triple-point region of the flow and hence, leading to unrealistic scenario of permanent pressure stabilisation at the triple point pressure (5.18 bar for CO_2).

In order to deal with the above limitation, a suitable estimate for non-zero speed of sound at the triple point is required. Accordingly, the Homogeneous Frozen Mixture (HFM) [11,29] assumption for speed of sound is adapted for three-phase mixture at the triple point as given by:

$$\forall k = v, l; \qquad \frac{1}{\rho c^2} = \sum_k \frac{y_k}{\rho_k c_k^2} \tag{13}$$

During numerical simulations, the fluid phase composition is determined at each time step as an outcome of density-energy (ρ-e) flash calculations. If the results show that the fluid is two-phase then its speed of sound is calculated using HEM approach, while if the fluid is three-phase (i.e. vapour-liquid-solid mixture at the triple point), then the HFM model is applied. As such, Eq. (13) effectively removes the singularity introduced by the HEM speed of sound prediction. The impact of this approximation on the predictions of the wave structure and furthermore, on the depressurisation of high-pressure CO_2 pipelines are presented and discussed in Section 4.

3. NUMERICAL METHOD

The above flow model is solved numerically using the finite volume Godunov's method [26,30],

with an appropriate Riemann solver to approximate the required interfacial fluxes [26]. In this

method, the Euler Eq. (6) are integrated over a control volume $[x_{i-1/2}, x_{i+1/2}]$ and the time interval

$[t_n, t_{n+1}]$ as depicted figure 3:

$$\int_{x_{i-1/2}}^{x_{i+1/2}} U(x,t_{n+1})dx = \int_{x_{i-1/2}}^{x_{i+1/2}} U(x,t_n)dx + \int_{t_n}^{t_{n+1}} F(U(x_{i-1/2},t)dt - \int_{t_n}^{t_{n+1}} F(U(x_{i+1/2},t))dt \qquad (14)$$

where $x_{i-1/2}$ and $x_{i+1/2}$ are the coordinates of two adjacent cell interfaces, $[i-1/2]$ and $[i+1/2]$
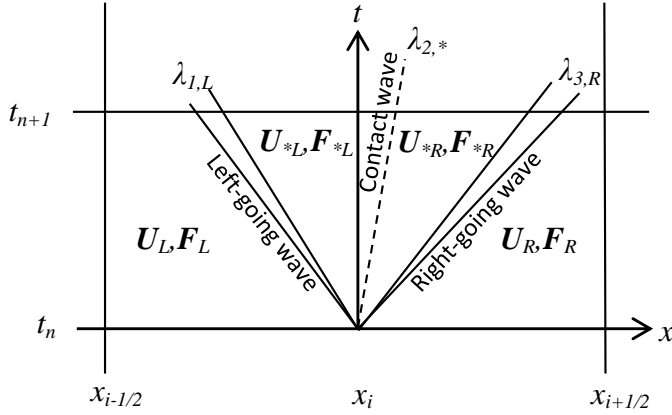
respectively.

Figure 3: Schematic representation of a wave configuration emerging in the ith cell of the discretised computational domain over the time interval $[t_n, t_{n+1}]$. Indices L and R refer respectively to the states on the left and on the right of the domain affected by wave propagation, while * corresponds to a "star region" bounded by the left- and right-going waves.

If the time step, $\Delta t = t_{n+1} - t_n$ satisfies the CFL condition:

$$CFL = \frac{\Delta t \left((|u \pm c|)_{max} \right)}{\Delta x} \leq 1 \qquad (15)$$

after some algebraic manipulation, Eq. (14) can be recast into:

$$U_i^{n+1} = U_i^n + \frac{\Delta t}{\Delta x} \left[F_{i-1/2} - F_{i+1/2} \right] \qquad (16)$$

where U_i is the vector of averaged conservative variables in $[x_{i-1/2}, x_{i+1/2}]$ and $F_{i\pm1/2}$ is the so-called Godunov's fluxes evaluated at the cell interfaces (indexed as $i\pm1/2$).

In the current work, the HLLC approximate Riemann solver [31] is used to compute the required Godunov's fluxes in order to advance the solution in time and space:

$$F_{i\pm1/2} = \begin{cases} F_L & , \text{if} & 0 \le S_L \\ F_L + S_L(U_{*L} - U_L) & , \text{if} & S_L < 0 < S_* \\ F_R + S_R(U_{*R} - U_R) & , \text{if} & S_* \le 0 < S_R \\ F_R & , \text{if} & 0 \ge S_R \end{cases} \tag{17}$$

where U_* is the vector of conservative variables in the 'star region' bounded by the fastest left-going (L) and right-going (R) waves (see figure 3) and S_* is the speed of contact discontinuity, which are respectively defined as [31]:

$$U_{*J} = \rho_J\left(\frac{S_J - u_J}{S_J - S_*}\right)\begin{bmatrix} 1 \\ S_* \\ \dfrac{E_J}{\rho_J} + (S_* - u_J)\left[S_* + \dfrac{p_J}{\rho_J(S_J - u_J)}\right] \end{bmatrix}, \quad (J = L, R) \tag{18}$$

$$S_* = \frac{p_R - p_L + \rho_L u_L(S_L - u_L) - \rho_R u_R(S_R - u_R)}{\rho_L(S_L - u_L) - \rho_R(S_R - u_R)} \tag{19}$$

In presence of heat transfer and friction, when the source term vector, $\boldsymbol{\Psi}$, in Eq. (1) is non-zero, its presence is accounted for in the numerical integration method using the fractional splitting technique [26].

4. RESULTS AND DISSCUSSIONS

4.1 Model verification. In order to verify the computational flow model developed above, a Riemann problem test is performed, where Eq. (6) is solved to obtain the flow profiles, numerically approximating the exact wave structure of the solution.

The simulation is performed for a 100 m long horizontal flow domain, initially filled with CO_2. The left half of the domain is set to be liquid at 30 bar, whilst the right half is set as vapour at 1 bar for the prevailing conditions as summarised in Table 1.

The flow domain is discretised uniformly into 2000 cells, and the CFL number is set at 0.5, found to be sufficient to guarantee convergence (see the gird convergence study results in figure 4).
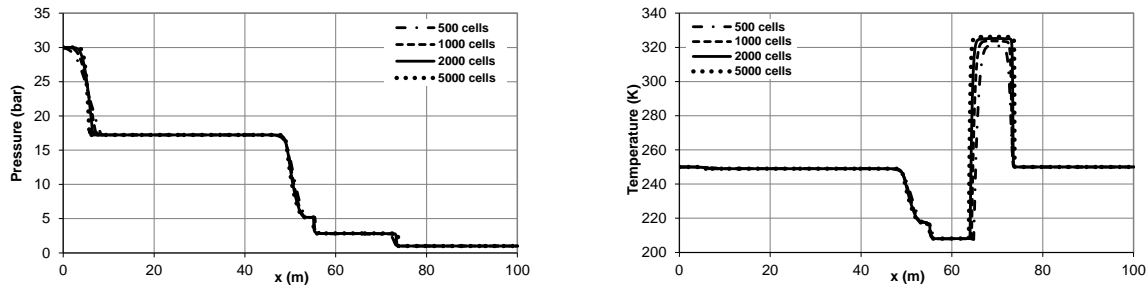
(a)   (b)

Figure 4: The pressure (a) and temperature (b) profiles predicted at 0.06 s using various numbers of cells for the Riemann problem test (Table 1).

Figure 5 depicts the flow pressure (figure 5a) and temperature (figure 5b) profiles at 0.06 s predicted using both Eq. (7) and (13) for predicting the fluid speed of sound at the triple point. Also included in figure 5a is a magnified plot for the dash-line boxed region of the pressure profile.
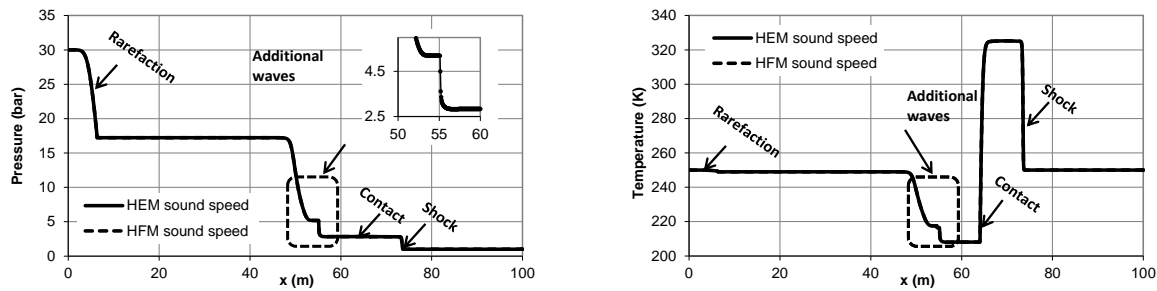
(a)   (b)

Figure 5: Variation of pressure (a) and temperature (b) along the flow domain in the Riemann problem test at 0.06 s.

Referring to figure 5, as it may be expected according to the classical solution (see figure 2), three simple waves emerge, including a rarefaction wave at ca. 5 m, a contact wave at ca. 65 m and a shock at ca. 75 m. The main features of these three classical waves are predicted consistently with the previous studies in gas dynamics [26]. In particular, across the rarefaction wave, all the flow properties change continuously and smoothly. Across the contact wave, there is a discontinuous change in the temperature (and other related thermal properties such as density and entropy) while the pressure and velocity remain constant. Across the shock wave, all the flow properties change discontinuously.

Interestingly, apart from these three waves, two additional waves respectively at ca. 50 m and 55 m can be observed in the left part of the domain (as marked by dashed-line box). They are separated from the most left rarefaction wave by two plateaux, respectively at ca. 17 bar (saturated vapour-liquid) and 5.18 bar (the triple point) pressures.

In order to verify the flow model predictions and relate these waves to the physical nature of the fluid (e.g. phase transitions), the prediction is then compared to the wave structure obtained from an analytical analysis of the isentrope (at the entropy value corresponding to the left part of the domain) in p-v plane following Menikoff and Plohr [18] (see Section 2.2).

Figure 6 shows p-v phase diagram for CO_2 with several isentropes crossing the two-phase equilibrium region and the triple point.
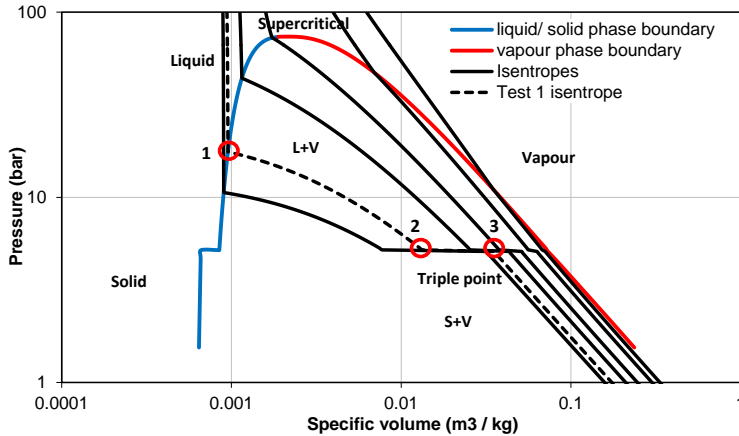
Figure 6: CO_2 p-v phase diagram, showing the phase boundaries and isentropes crossing the phase equilibria regions; following Test 1 isentrope, the points where phase transition occurs are sequentially marked as point 1, 2 and 3 and circled in red.

Focusing on the isentrope presented by the dashed line in figure 6, three points exist at which its slope changes discontinuously. In the order of appearance these include at the phase transition boundaries of liquid-vapour (point 1), the triple point (point 2), and solid-vapour (point 3).

Figure 7 shows the calculated fundamental derivative, ς along this isentrope. It can be seen that ς vanishes at point 1, 2 and 3, indicating formation of anomalous waves.
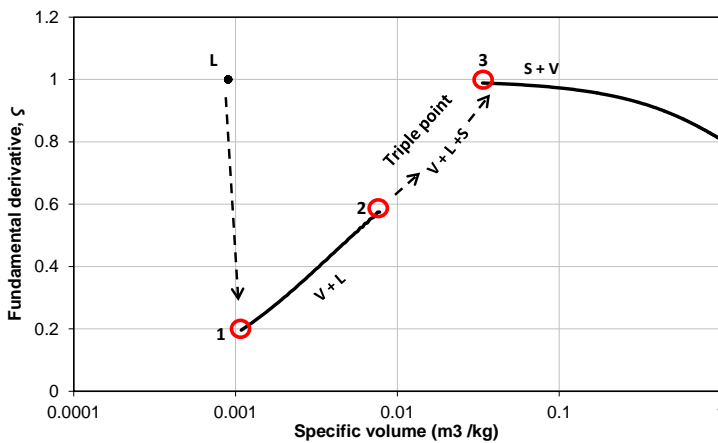

Figure 7: Fundamental derivative, ς (defined by Eq. (8)) along the isentrope of Test 1; phase transition boundaries are marked and circled in red.

To determine the type of the anomalous waves emerging at these three points, the convexity of the isentrope across these points is examined. Referring to figure 7, on both sides of point 1 (e.g.

15

pure liquid and vapour-liquid phases), ς remains positive, and the convexity of the isentrope is preserved. As such, at this phase transition boundary, the emerging wave can be classified as a split rarefaction wave from the rarefaction wave at ca. 5 m (see figure 5).

As also can be seen in figure 7, in contrast to point 1, ς vanishes both at and between points 2 and 3 where the fluid remains at the triple point. As such, the analysis applied above to reveal the type of anomalous wave at point 1 cannot be directly extended to the phase transition boundaries at points 2 and 3. Alternatively, the nature of these waves may be interpreted by looking at the variation of the wave propagation speeds near the triple point.
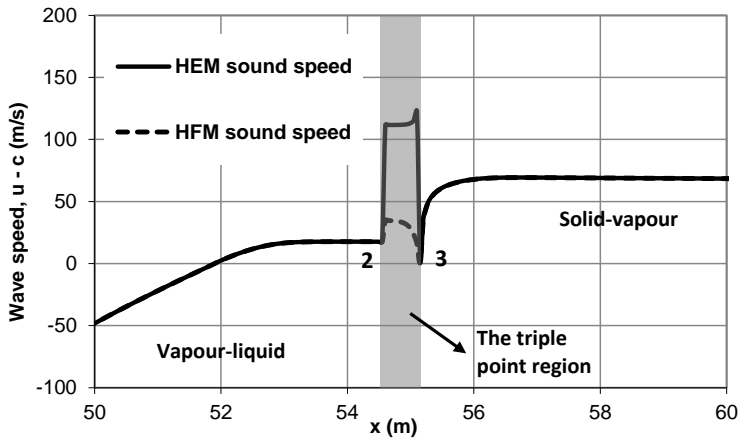

Figure 8: Variation of the wave speed in the flow near the triple point (conditions of figure 5) obtained by both speed of sound approaches.

Figure 8 shows the wave speed profiles corresponding to figure 5 in the proximity of the triple point. As can be seen in figure 8 for both speed of sound models, the predicted wave speeds only differ within the triple pint region (as expected). The predicted wave speed beyond phase transition boundary at point 3 (in the solid-vapour mixture) increases rapidly and becomes significantly larger than that at point 2. This gives rise to the second rarefaction wave split at ca. 55 m, as can be observed in figure 5. Returning to figure 8, given that at the triple point the pressure and temperature remain constant (as the fluid has zero thermodynamic degree of freedom), the different wave speeds predicted by the two models can be expected to have no

impact on the solution of the Riemann problem. This is supported by a comparison between the predicted pressure and temperature profiles presented in figure 5, showing overlapped results.

The wave structure resulting from the above analysis is summarised in figure 9, where the contact and shock waves are also included for completeness.
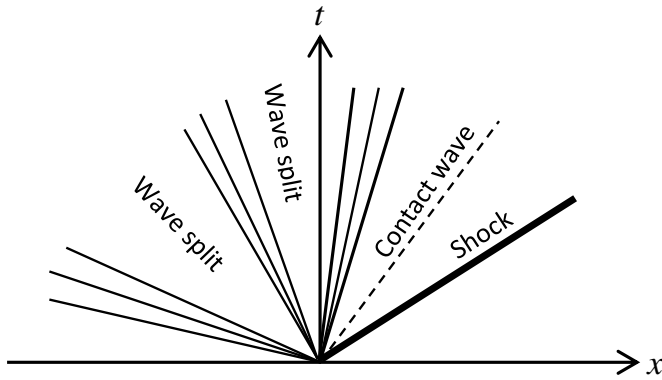

Figure 9: Wave structure of the hyperbolic system with fluid phase transition across the vapour-liquid region and the triple point.

It is also worth noting that the isentropes originating either in the liquid (dense) or supercritical phases all exhibit discontinuous changes at the previously discussed phase transition boundaries (see figure 6). Given that CO_2 is normally transported in the dense or supercritical phases (i.e above 73 bar) due to economic considerations, the numerically discovered anomalous waves associated with solid CO_2 formation is thus expected during complete decompression of CO_2 transportation pipelines.

4.2 Model Experimental Validation. In the following, the flow model presented above is validated against measurements taken from a large-scale pipeline decompression experiment performed as part of the COOLTRANS UK National Grid project [32]. The test involved the Full Bore Rupture (FBR) of a thermally insulated 144 m long, 150 mm i.d. and 11 mm wall thickness steel pipe containing dense-phase CO_2 initially at 5.25 $^{\circ}$C (278.38 K) and 153.3 bar. The pipe

was instrumented with fast response pressure and temperature transducers strategically placed along its length. The full details of the test set-up can be found in reference [33].

Simulations are performed based on a computational domain of 500 discretised cells (further grid refinement produces little variance in the results) and using a CFL number of 0.5.

Figure 10 shows the predicted and measured variations of pressure with time at the intact end of the test pipe following its FBR using an explosive charge.
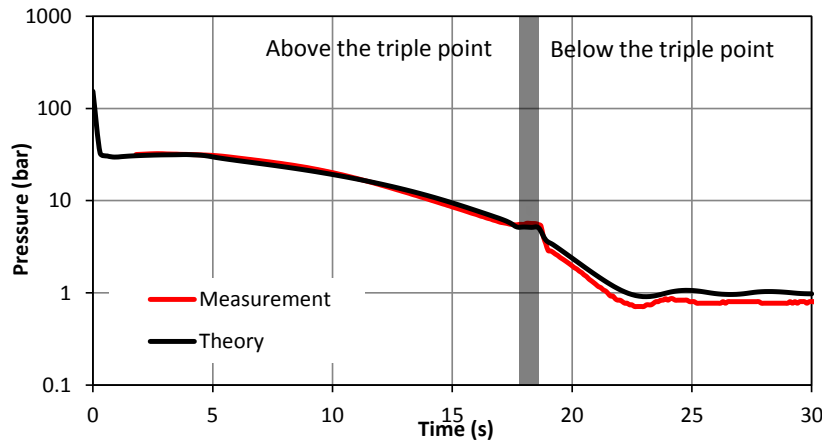

Figure 10: The variation of CO_2 intact end pressure with time following FBR The shaded area shows the triple point location.

As it may be observed, theory and experiment are in excellent agreement. The initial rapid drop in pressure from 153.3 to 30 bar synonymous with FBR is followed by temporarily pressure stabilisation at ca. 30 bar lasting for ca. 4.5 s. The latter corresponds to the split of the rarefaction wave at the vapour-liquid phase transition boundary (see Section 4.1).

Following this temporary stabilisation, the pressure gradually decreases until ca. 18 s, where a second pressure plateau is observed at the CO_2 triple point (5.18 bar). This is attributed to the additional split of the rarefaction wave at the triple point phase transition boundary. As can be further observed from figure 10, after ca 18 s, the depressurisation of two-phase solid-vapour mixture proceeds until reaching the ambient pressure.
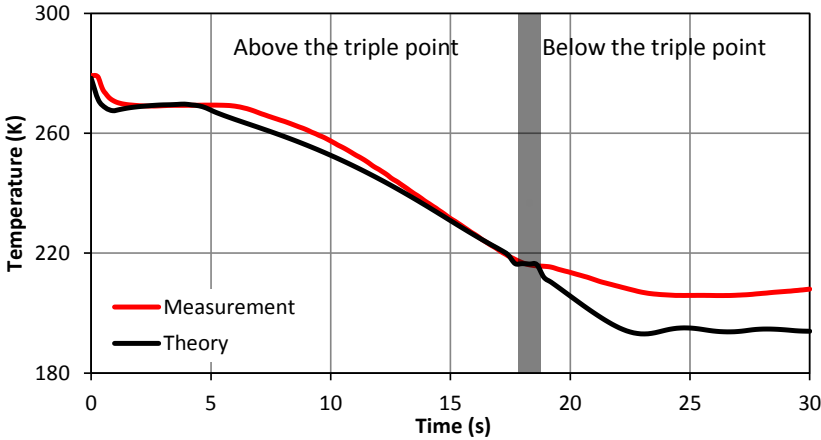
Figure 11: The variation of CO_2 intact end temperature with time following FBR. The shaded area shows the triple point location.

Figure 11 shows the corresponding variations of intact end temperature with time following FBR based on measurements and model predictions. As it may be observed, the temperature profiles follow very similar trends as with the pressure profiles presented and discussed in figure 10. However, although theory and experiment are in good accord up to the triple point region, the degree of agreement decreases beyond this point where the flow model under-predicts the CO_2 temperature by as much as ca. 12 K.

We postulate that the observed discrepancy is mainly a consequence of the extent of the validity of the HEM assumption embedded in the flow governing Eq. (1) in which the constituent fluid phases are assumed to be at thermal equilibrium and travel at the same velocity. Prior to crossing the CO_2 triple point, the observed reasonably good agreement between theory and experiment indicates that such an assumption holds in this region. This is most likely due to the relatively high momentum and thus good mixing of the liquid and vapour phases such that inhomogeneity would be expected to be insignificant, i.e. the flow is fully dispersed.

However, the passing of the triple point marks the formation of much denser solid CO_2 which separates and settles out of the vapour/solid mixture due the gravitational field effect thus invalidating the HEM assumption. Additionally, due to the low heat capacity of the separated

vapour phase, the fluid/wall heat transfer may result in superheated vapour (instead of saturated vapour predicted by the present model). Given that in the current study the fluid phase separation is not accounted in the heat transfer model, this may also contribute to the discrepancy observed between the present model temperature predictions and the measured data.

Figure 12 shows the variation of solid mass fraction along the pipe at different times of 15.6, 17.4 and 19.2 s following FBR. The data indicate that by 15.6 s following rupture, approximately 35% of the total mass of the remaining CO_2 at the rupture plane (140 m) is in solid phase with the rest of the content upstream remaining in vapour phase. By 17.4 s following rupture (i.e. 2.4 s later), the solid front has propagated by approximately 30 m, reaching the pipe intact end at 19.2 s following rupture, where the percentage solid along the entire pipe length is approximately 30%.

As mentioned earlier, the solid-vapour phase separation is not accounted for in the current HEM flow model and, thus, the predicted distribution of the solid CO_2 along the length of the pipe may be inaccurate. However, we may expect the HEM approximation to be applicable at the point of phase transition from liquid-vapour to vapour-liquid-solid at the triple point (i.e. at the 'solid front'), providing valid estimates for the solid front propagation and the amount of solid CO_2 formed behind. Such information is vitally important as it directly governs the likelihood of pipeline or emergency blowdown valve blockage.
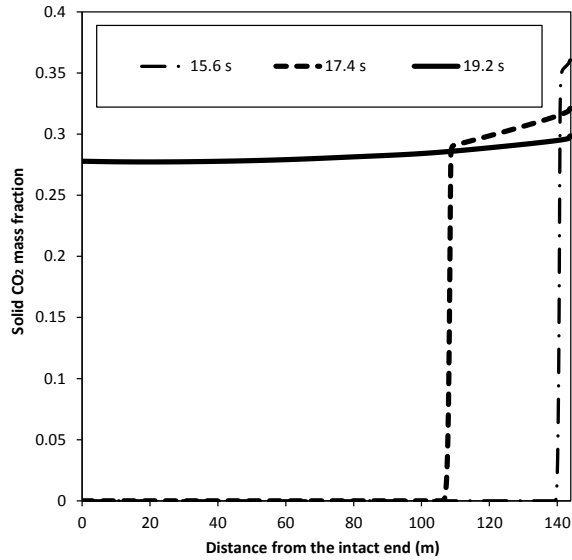
Figure 12: Variation of predicted solid phase CO_2 mass fraction along the pipeline at different times during the depressurisation.
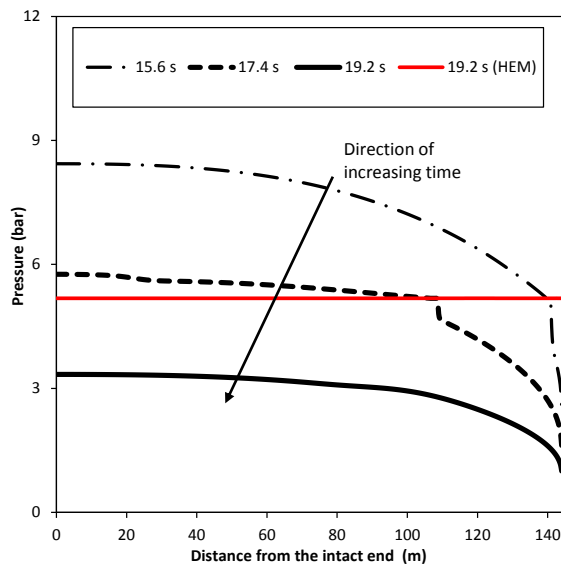

Figure 13: Variation of predicted pressure along the pipeline at different times during the depressurisation.

Figure 13 shows the corresponding variation of the predicted pressure profiles along the pipeline following FBR at the same times as those in figure 12. The data based on the speed of sound calculated using the Eq. (7) (as opposed to Eq. (13)) at 19.2 s following FBR is also included indicating an unrealistic constant pressure throughout the entire pipeline length at the

triple point pressure (5.17 bar). In contrast the proposed model produces the expected rapid drop in pressure at the rupture plane which gradually stabilises with distance towards the pipe intact end. The rapid drop in pressure which can be observed in the profiles at 15.6 s and 17.4 s in figure 13, again correspond to the phase transition from the triple point state to the solid-vapour two-phase equilibrium.

5. CONCLUSIONS AND FUTURE WORK

It is widely recognised that as part of the CCS chain, high-pressure transmission pipelines represent the most practical and economic way of transporting the captured CO_2 from coal fired power plants and other CO_2 intensive industries for subsequent sequestration. Given the hazardous nature of CO_2, the significant quantities transported and the inevitable likelihood of such pipelines passing near or through populated areas, their safe operation is of paramount importance.

This paper for the first time presented the development, testing and validation of a rigorous decompression flow model for predicting the quantity of solid CO_2 formed as a function of time and distance along high-pressure pipelines during decompression. In practice, such predictive capability is important for a number of safety and operational reasons. These include pressure relief valve sizing, appropriate pipeline design in order to avoid blockage and minimising the risk of exposure of personnel to high doses of undiscovered accumulated sublimating solid CO_2 following pipeline depressurisation for maintenance purposes.

The flow model developed was based on the solution of the mass, energy and momentum conservation equations, accounting for fluid/wall heat transfer and frictional effects. The pertinent thermodynamic and phase equilibrium data for CO_2 above and below its triple point were computed using the GERG 2004 EoS and the ePR EoS respectively. A Homogenous

Frozen Model was implemented for predicting the speed of sound of the multiphase mixture at and below the CO_2 triple point.

For model verification, a numerical approximation of the wave structure in the vapour-liquid-solid flow was demonstrated by performing a Riemann problem test. Anomalous waves were predicted by the flow model, consisting of two split rarefaction wave splits at the vapour-liquid and the triple point phase transition boundaries.

The flow model was next validated against the pressure and temperature measurements obtained from a large-scale CO_2 pipeline FBR decompression test performed during the course of the COOLTRANS project [32].

Indicating generally good agreement with the measured data, the model successfully reproduced the observed temporal pressure plateau at the triple point. Typical data generated using the model included the variations of pressure, temperature and solid mass fraction along the pipe as a function of time during its decompression. As to be expected, the amount of solids increased with distance towards the rupture plane; picking at a maximum value of 35% for the conditions tested.

It should be noted that the flow model presented in this study is based on the HEM assumption where the constituent fluid phases are assumed to be at thermal and mechanical equilibrium; the latter implying no phase slip. In practice, the marked differences between the densities of solid and vapour CO_2 means that this assumption will become less valid below the CO_2 triple point particularly when the depressurisation rate decreases. Here, the inertia of the flowing fluid may not overcome the gravitation field effect ultimately resulting in the disengagement and eventual settling of the accompanying solid CO_2. The subsequent impact was clearly demonstrated in the

present study in the form of the observed finite disagreement between the recorded and predicted fluid temperatures below the CO_2 triple point.

Additionally, in practice, depending on the capture technology employed, CO_2 streams may contain different types and amounts of impurities. Some of these have already been shown to have a marked impact to CO_2 phase equilibrium behaviour above its triple point even when present in small quantities [13].

Future work will involve the extension of the present work to account for phase slip and the impact of CO_2 impurities on the extent of solid formation during the decompression of CO_2 pipelines.

Table 1: Initial conditions of CO_2 in left and right part of the computational domain in the Riemann problem test.

Fluid property	Left state (x<50 m)	Right state (x>50m)
Pressure, bar	30	1
Temperature, K	250	250
Fluid phase	Liquid	Vapour

AUTHOR INFORMATION

Corresponding Author

*E-mail: h.mahgerefteh@ucl.ac.uk.

ABBREVIATIONS

CCS, Carbon Capture and Sequestration; ePR EoS, extended Peng-Robinson Equation of State; HEM, Homogeneous Equilibrium Model; HFM, Homogeneous Frozen Model.

REFERENCES

(1)   Lindstrom, P. *International Energy Outlook 2016, Carbon Dioxide Emissions*; Washington, D.C., 2016.

(2)   Woolley, R. M.; Fairweather, M.; Wareing, C. J.; Falle, S. A. E. G.; Mahgerefteh, H.; Martynov, S.; Brown, S.; Narasimhamurthy, V. D.; Storvik, I. E.; Sælen, L.; Skjold, L.; Economou, I. G.; Tsangaris, D.M.; Boulougouris, G. C.; Diamantonis, N.; Cusco, L.; Wardman, M.;Gant, S. E.; Wilday, J.; Zhang, Y. C.; Chen, S. Y.; Proust, C.; Hebrard, J.; Jamois, D. CO2PipeHaz: Quantitative Hazard Assessment for next Generation CO_2 Pipelines. *Energy Procedia* **2014**, *63*, 2510.

(3)   Harper, P.; Wilday, J.; Bilio, M. Assessment of the major hazard potential of carbon dioxide (CO_2) http://www.hse.gov.uk/carboncapture/assets/docs/major-hazard-potential-carbon-dioxide.pdf (accessed Dec 20, 2016).

(4)   Mikalauskas, K.; Urba, E.; Miškūnas, P.; Smirnov, D.; Burokas, A.; Miškinis, R. Realization of the Sublimation Temperature Point of Carbon Dioxide. *Lith. J. Phys.* **2013**, *53*, 127.

(5)   Jensen, M. D.; Schlasner, S. M.; Sorensen, J. A.; Hamling, J. A. Operational Flexibility of CO_2 Transport and Storage. *Energy Procedia* **2014**, *63*, 2715.

(6)   Eldevik, F.; Graver, B.; Torbergsen, L. E.; Saugerud, O. T. Development of a Guideline for Safe, Reliable and Cost Efficient Transmission of CO_2 in Pipelines. *Energy Procedia* **2009**, *1*, 1579.

(7)   Huang, D.; Quack, H.; Ding, G. L. Experimental Study of Throttling of Carbon Dioxide Refrigerant to Atmospheric Pressure. *Appl. Therm. Eng.* **2007**, *27*, 1911.

(8)   Koh, C. A.; Westacott, R. E.; Zhang, W.; Hirachand, K.; Creek, J. L.; Soper, A. K. Mechanisms of Gas Hydrate Formation and Inhibition. *Fluid Phase Equilib.* **2002**, *194-197*, 143.

(9)   Buit, L.; Ahmad, M.; Mallon, W.; Hage, F. CO_2 EuroPipe Study of the Occurrence of Free Water in Dense Phase CO_2 Transport. *Energy Procedia* **2011**, *4*, 3056.

(10)   Woolley, R. M.; Fairweather, M.; Wareing, C. J.; Falle, S. A. E. G.; Proust, C.; Hebrard, J.; Jamois, D. Experimental Measurement and Reynolds-Averaged Navier–Stokes Modelling of the near-Field Structure of Multi-Phase CO_2 Jet Releases. *Int. J. Greenh. Gas Control* **2013**, *18*, 139.

(11)   Brown, S.; Martynov, S.; Mahgerefteh, H.; Proust, C. A Homogeneous Relaxation Flow Model for the Full Bore Rupture of Dense Phase CO_2 Pipelines. *Int. J. Greenh. Gas Control* **2013**, *17*, 349.

(12)   Brown, S.; Martynov, S.; Mahgerefteh, H.; Chen, S.; Zhang, Y. Modelling the Non-Equilibrium Two-Phase Flow during Depressurisation of CO_2 Pipelines. *Int. J. Greenh. Gas Control* **2014**, *30*, 9.

(13)   Mahgerefteh, H.; Brown, S.; Martynov, S. A Study of the Effects of Friction, Heat Transfer, and Stream Impurities on the Decompression Behavior in CO_2 Pipelines. In *Greenhouse Gases: Science and Technology*; 2012; Vol. 2, pp 369–379.

(14)   Teng, L.; Li, Y.; Zhao, Q.; Wang, W.; Hu, Q.; Ye, X.; Zhang, D. Decompression Characteristics of CO_2 Pipelines Following Rupture. *J. Nat. Gas Sci. Eng.* **2016**, *36*, 213.

(15)   Martynov, S.; Brown, S.; Mahgerefteh, H.; Sundara, V.; Chen, S.; Zhang, Y. Modelling Three-Phase Releases of Carbon Dioxide from High-Pressure Pipelines. *Process Saf. Environ. Prot.* **2014**, *92*, 36.

(16)   Martynov, S.; Brown, S.; Mahgerefteh, H. An Extended Peng-Robinson Equation of State for Carbon Dioxide Solid-Vapor Equilibrium. *Greenh. Gases Sci. Technol.* **2013**, *3*, 136.

(17)   Hammer, M.; Ervik, A.; Munkejord, S. T. Method Using a Density-Energy State Function with a Reference Equation of State for Fluid-Dynamics Simulation of Vapor-Liquid-Solid Carbon Dioxide. *Ind. Eng. Chem. Res.* **2013**, *52*, 9965.

(18)   Menikoff, R.; Plohr, B. J. The Riemann Problem for Fluid Flow of Real Materials. *Rev. Mod. Phys.* **1989**, *61*, 75.

(19) Munkejord, S. T.; Hammer, M.; Løvseth, S. W. CO_2 Transport: Data and Models - A Review. *Appl. Energy* **2016**, *169*, 499.

(20) Stadtke, H. *Gasdynamic Aspects of Two-Phase Flow*; Wiley-VCH: Weinheim, 2006.

(21) Chen, N. H. An Explicit Equation for Friction Factor in Pipes. *Int. Eng. Chem. Fundam.* **1979**, *18*, 296.

(22) Mahgerefteh, H.; Wong, S. M. A Numerical Blowdown Simulation Incorporating Cubic Equations of State. *Comput. Chem. Eng.* **1999**, *23*, 1309.

(23) Haque, M. A.; Richardson, S. M.; Saville, G. Blowdown of Pressure Vessels Part I. Computer Model. *Trans IChemE* **1992**, *70*, 3.

(24) Incropera, F. P.; De Witt, D. P. *Fundamentals of Heat and Mass Transfer*, 2nd ed.; John Wiley & Sons: New York, 1985.

(25) Lemmon, E. W.; Huber, M. L.; McLinden, M. O. NIST Standard ReferenceDatabase 23: Reference Fluid Thermodynamic and Transport Properties - REFPROP. NIST 2010.

(26) LeVeque, R. J. *Finite Volume Methods for Hyperbolic Problems*; Cambridge University Press: Cambridge, 2002.

(27) Munkejord, S. T.; Hammer, M. Depressurization of CO_2-Rich Mixtures in Pipes: Two-Phase Flow Modelling and Comparison with Experiments. *Int. J. Greenh. Gas Control* **2015**, *37*, 398.

(28) Kunz, O.; Wagner, W. The GERG-2008 Wide-Range Equation of State for Natural Gases and Other Mixtures: An Expansion of GERG-2004. *J. Chem. Eng. Data* **2012**, *57*, 3032.

(29) Nouri-Borujerdi, A.; Shafiei Ghazani, A. Equilibrium and Non-Equilibrium Gas–liquid Two Phase Flow in Long and Short Pipelines Following a Rupture. *AIChE J.* **2017**, *63*, 3214.

(30) LeVeque, R. J. *Numerical Methods for Conservation Laws*, 2nd ed.; Birkhauser Verlag: Basel, 1992.

(31) Toro, E. F. The HLL and HLLC Riemann Solvers. In *Riemann Solvers and Numerical Methods for Fluid Dynamics*; Springer: Heidelberg, 2009; pp 293–311.

(32) Brown, S.; Martynov, S.; Mahgerefteh, H. A Coupled Two-Phase Flow Model for Predicting the Flashing of Liquid CO_2 during Pipeline Decompression. In *Turbulence, Heat and Mass Transfer 8*; Hanjalic, K., Miyauchi, T., Borello, D., Habziabdic, M., Venturini, P., Eds.; Begell House, Inc: Sarajevo, Bosnia and Herzegovina, 2015; pp 1–12.

(33) Cosham, A.; Jones, D. G.; Armstrong, K.; Allason, D.; Barnett, J. The Decompression Behaviour of Carbon Dioxide in the Dense Phase. *Proc. 2012 9th Int. Pipeline Conf.* **2012**, 447.

LIST OF FIGURE CAPTIONS

Figure 1: Photographs of the release end of the CO2PipeHaz blowdown test pipeline (a) and lumps of solid CO_2 formed within the pipe in the FBR test (b). Photographs courtesy of Dalian University of Technology.

Figure 2: Schematic representation of the classical wave structure from solving the Euler equation of gas dynamics.

Figure 3: Schematic representation of a wave configuration emerging in the ith cell of the discretised computational domain over the time interval $[t_n, t_{n+1}]$. Indices L and R refer respectively to the states on the left and on the right of the domain affected by wave propagation, while * corresponds to a "star region" bounded by the left- and right-going waves.

Figure 4: The pressure (a) and temperature (b) profiles predicted at 0.06 s using various numbers of cells for the Riemann problem test (Table 1).

Figure 5: Variation of pressure (a) and temperature (b) along the flow domain in the Riemann problem test at 0.06 s.

Figure 6: CO_2 p-v phase diagram, showing the phase boundaries and isentropes crossing the phase equilibria regions; following Test 1 isentrope, the points where phase transition occurs are sequentially marked as point 1, 2 and 3 and circled in red.

Figure 7: Fundamental derivative, ς along the isentrope of Test 1; phase transition boundaries are marked and circled in red.

Figure 8: Variation of the wave speed in the flow near the triple point (conditions of figure 5) obtained by both speed of sound approaches.
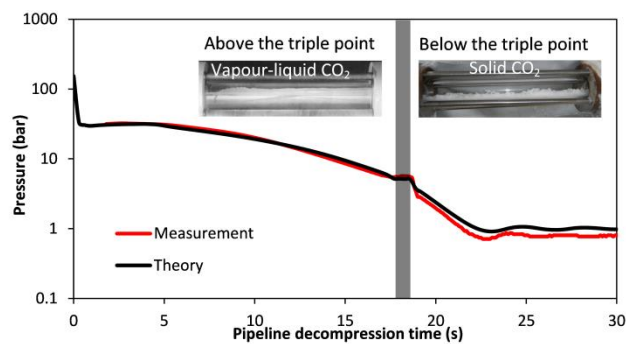
Figure 9: Wave structure of the hyperbolic system with fluid phase transition across the vapour-liquid region and the triple point.

Figure 10: The variation of CO_2 intact end pressure with time following FBR The shaded area shows the triple point location.

Figure 11: The variation of CO_2 intact end temperature with time following FBR. The shaded area shows the triple point location.

Figure 12: Variation of predicted solid phase CO_2 mass fraction along the pipeline at different times during the depressurisation.

Figure 13: Variation of predicted pressure along the pipeline at different times during the depressurisation.

For Table of Contents Only.